Research Square

Preprints are preliminary reports that have not undergone peer review.
They should not be considered conclusive, used to inform clinical practice,
or referenced by the media as validated information.

Using Cellulose Nanofibers as the Sole Binder for Cement-Free Construction Materials

Małgorzata Szafraniec

m.szafraniec@pollub.pl

Lublin University of Technology

Linfei Li

Florida International University

Eric N. Landis

University of Maine

Article

Keywords: cellulose nanofibers, cement-free composites, sustainable construction, compressive strength, hydrogen bonding, nanocellulose binder

Posted Date: September 16th, 2026

DOI: https://doi.org/10.21203/rs.3.rs-10921521/v1

License: This work is licensed under a Creative Commons Attribution 4.0 International License.
Read Full License

Additional Declarations: No competing interests reported.

Version of Record: A version of this preprint was published at Scientific Reports on November 13th, 2026. See the published version at https://doi.org/10.1038/s41598-026-78922-3.

Abstract

Cement production is one of the largest industrial sources of carbon dioxide, which has intensified interest in binders that are renewable and low in embodied carbon. Cellulose nanofibers (CNF), fine fibrils extracted from wood, bind strongly through hydrogen bonding and have long served as adhesives in wood-based panels, but they had not previously replaced cement entirely in mineral-aggregate composites. Here we report the first systematic study in which CNF serves as the sole binder for sand, with no cement present. Twelve compositions were prepared across a broad range of cellulose contents and cellulose-to-sand ratios. Cohesive solid specimens formed once the cellulose content exceeded a threshold, and their dry compressive strength ranged from 0.42 to 3.73 MPa, comparable to rammed earth and adobe. Strength was governed mainly by the total amount of dry cellulose rather than by packing density. Saturating the specimens with water reduced their strength almost to zero, but re-drying fully restored, and slightly exceeded the original strength, showing that the binding is a reversible physical process rather than a permanent chemical set. These results establish the feasibility and basic property landscape of cement-free CNF-sand composites and point toward lightweight, low-carbon, and potentially recyclable non-structural materials.

1. Introduction

In the construction industry, concrete is the most widely consumed material, accounting for about 8% of global CO_2 emissions [1]. While cement comprises only around 10–15% of concrete by mass, it contributes over 90% of the total CO_2 emissions from concrete production [2]. This disproportionate contribution arises from two approximately equal sources: energy consumption and limestone decomposition, each contributing approximately 50% to cement's carbon footprint [1, 2]. In traditional concrete production, cement plays a critical role as the 'glue' that binds the matrix together. When cement reacts with water, it forms calcium silicate hydrate (C-S-H) and other chemical phases that provide sufficient bonding to the surrounding aggregates, which are generally considered inert fillers [3]. Current projections show that global cement demand will continuously increase by 48%, from 4.2 billion tons to 6.2 billion tons by 2050 [4]. While the use of green energy sources offers significant potential for reducing the carbon footprint of cement production, the direct CO_2 emissions from the conversion of limestone to quicklime are unavoidable, creating a significant gap in achieving carbon neutrality within the construction sector.

In response, growing attention has been paid to the development of new types of 'concrete' using alternative binders, including Portland limestone cement (PLC), magnesium-based cement, ternary blend cement, geopolymers, limestone calcined clay cement (LC3), and bio-cement [5]. However, none of these alternatives fully eliminates the use of cementitious materials. Wood-based materials have been recognized as a sustainable feedstock for various products. The U.S. wood product market reached $284.7 billion in 2023 and is expected to continue growing [6]. However, complex biological structure leads to inconsistent quality, particularly in the Northeast region, where over 70–80% of the wood is considered low-quality, limiting applications to packaging, decoration, landfill disposal, or firewood [7].

Cellulose nanomaterials (CNMs), including cellulose nanofibers (CNF), cellulose microfibrils (CMF), and cellulose nanocrystals (CNC), have emerged as valuable products widely utilized across biomedical, coatings, papermaking, electronics, and agricultural industries [8–11]. Despite this potential, the application of CNMs in the construction industry remains extremely limited and no commercial-scale deployment has occurred [12, 13]. Current lab-scale studies suggest that CNMs can be added to concrete in amounts typically less than 0.75 cwt%, offering modest improvements in mechanical performance, shrinkage mitigation, rheology modification, and microstructure refinement, but without fundamentally displacing cement [14–17].

According to the manufacturer's Safety Data Sheet (CAS 9004-34-6), the CNFs used in this study exhibit fiber-like morphology with widths of 5-200 nm, lengths vary from 130 nm to 225 μm, aspect ratios of 14–23, crystallinity of 67–88%, thermal stability up to approximately 305°C, neutral pH, zeta potential of -48 to -5 mV, and decomposition temperature above 349°C [18]. These properties, particularly the high surface area and abundant hydroxyl groups capable of forming extensive hydrogen bonds, suggest potential as a matrix binder for mineral aggregates.

Previous studies by Tajvidi et al. demonstrated the feasibility of using CNF as the sole binder, without synthetic adhesives, for wood-based particleboard, for which a patent was granted [19–21]. However, extension of this binding concept from wood particles to mineral aggregates such as sand has not previously been explored. No peer-reviewed study has reported the complete replacement of cement with CNF as the sole binder for sand-based composites. The present study therefore provides the first systematic, published investigation into cement-free composites where CNF entirely replaces cement as the matrix binder for sand aggregates. Given the complete absence of prior data in the open literature, the study was designed as an exploratory program to map the broadest possible composition space and identify governing parameters, providing a foundation for subsequent optimization.

2. Results and Discussion

2.1. Dimensional stability and drying behavior

All 12 primary compositions produced cohesive specimens. Sample S317-15 (15:85 ratio) disintegrated, establishing ~ 25% (0.75 eff%) CNF as the minimum for cohesion. Weight loss ranged from 24.1% to 49.0%, correlating with CNF content (Pearson correlation: $r = 0.989$, $p < 0.001$). Dimensional shrinkage was strongly ratio-dependent: 25% CNF showed 1.3% average length decrease; 50% CNF showed 12% length, 11.3% width, and 10.7% height reduction (Supplementary Table S2). This is consistent with volumetric contraction behavior of nanocellulose gels [22]. Photographs of all specimens are provided in Supplementary Figures S1-S2.

2.2. Repeatability and effect of sand grain size

Replicate batches (S317-25R/40R/50R) showed CS differences of 14.1% and 8.1% for 40:60 and 50:50 ratios (two-sample *t*-test: $p = 0.39$, 0.34, not significant). The 25:75 ratio showed a significant difference

(two-sample *t*-test: $p = 0.018$), attributable to lower absolute CNF content increasing sensitivity to mixing variability. Mean CV across all CS measurements: 5.9% (range 0.9–20.7%). Fine sand specimens (S317-25F/40F/50F) showed consistently higher CS (+ 3.5–44.4%) but without statistical significance (two-sample *t*-test: $p = 0.097–0.358$). Both sets were excluded from the primary factorial analysis but are reported in Supplementary Table S3.

2.3. Compressive strength of dry specimens

Dry CS ranged from 0.42 ± 0.03 MPa (S317-25) to 3.73 ± 0.10 MPa (S587-50) (Table 2, Fig. 1). One-way ANOVA confirmed CNF content as the dominant factor ($F = 11.50$, $p = 0.003$). Post-hoc *t*-tests: 25% vs. 40% ($p = 0.007$), 25% vs. 50% ($p = 0.004$), 40% vs. 50% ($p = 0.096$). CNF solids alone was not significant (one-way ANOVA: $F = 0.575$, $p = 0.647$).

Table 2
Compressive strength (CS, $n = 3$, mean ± SD) and flexural strength (FS, $n = 1$) of dry specimens.

Sample	CNFeff [%]	CS ± SD [MPa]	CV [%]	FS [MPa]	FS/CS
S300-25	0.75	0.53 ± 0.01	1.1	0.13	0.25
S300-40	1.20	1.16 ± 0.04	3.3	0.35	0.30
S300-50	1.50	1.85 ± 0.09	4.6	0.67	0.36
S317-25	0.79	0.42 ± 0.03	6.3	0.07	0.17
S317-40	1.27	1.23 ± 0.06	4.9	0.42	0.34
S317-50	1.58	1.92 ± 0.10	5.3	0.79	0.41
S398-25	0.99	0.66 ± 0.07	10.8	0.13	0.20
S398-40	1.59	1.43 ± 0.06	4.4	0.40	0.28
S398-50	1.99	2.45 ± 0.14	5.8	0.85	0.35
S587-25	1.47	0.53 ± 0.11	20.7	0.03	0.06
S587-40	2.35	2.20 ± 0.02	0.9	0.56	0.25
S587-50	2.94	3.73 ± 0.10	2.6	1.17	0.31

Multiple regression: $CS = -2.84 + 0.077 \times CNF_{content} + 0.348 \times CNF_{solids}$ ($R^2 = 0.886$, adjusted $R^2 = 0.86$). The most parsimonious predictor was CNF_{eff} (linear regression; Pearson $r = 0.928$, $R^2 = 0.86$, $p < 0.001$): $CS = 1.428 \times CNF_{eff} - 0.683$ (Fig. 2). This indicates that the total dry cellulose available for hydrogen bonding fundamentally governs mechanical performance. The observed values (0.42–3.73 MPa) are comparable to rammed earth (0.5-5 MPa) and adobe (1–4 MPa) but below ordinary Portland cement (OPC) concrete (> 20 MPa) [3, 23, 24]. The strength trajectory shows no plateau with increasing CNF_{eff}, suggesting further improvements are achievable. Higher CNF_{eff} values were not explored here because

solids contents above ~ 6.0 wt% were unattainable under the present formulation methodology (see Methods); accessing this regime will require alternative dewatering or shaping routes.

2.4. Cellulose nanofiber alignment and mechanical anisotropy

Loading specimens perpendicular to the tamping direction (CS, standard) and parallel to it ($CS_{DiffDir}$) gave systematically different strengths. Across all 12 compositions, $CS_{DiffDir}$ exceeded the standard CS by a mean factor of 1.47 ± 0.29 (paired *t*-test: $p = 0.0003$), confirming that the composites are mechanically anisotropic (Supplementary Figure S3). The effect is consistent with preferential alignment of the high-aspect-ratio fibrils within the compaction plane: during tamping, fibrils reorient perpendicular to the applied force, so that loading along the fibril plane mobilises more inter-fibril hydrogen bonds than loading across it [25, 26]. Similar densification-driven strengthening through inter-fibril hydrogen bonding has been reported for binderless, compression-molded cellulose materials [25, 27]. This directional dependence should be considered when orienting these materials in use, and is a factor that future component-scale studies will need to control.

2.5. Effect of water: evidence for hydrogen bonding mechanism

Water saturation (WA + CS) reduced CS to 0.03–0.14 MPa with mean retention 5.8 ± 2.2% (Table 3, Fig. 3). This near-total loss confirms hydrogen bond-dependent binding: water molecules compete for hydroxyl groups on cellulose chains, dissolving the bonding network [28].

Table 3
Effect of water and drying cycles on CS. Ret. = retention (WA + CS/CS × 100%); Rec. = recovery ($WA+Oven_{CS}$/CS × 100%). All values in MPa unless noted.

Sample	CS	WA + CS	Ret. [%]	$WA+Oven_{CS}$	Rec. [%]	H + WA+Oven
S300-25	0.53	0.04	7.6	0.68	129	0.75
S300-40	1.16	0.05	4.3	1.47	126	1.55
S300-50	1.85	0.07	3.8	2.62	142	2.86
S317-25	0.42	0.05	11.9	0.35	83	0.74
S317-40	1.23	0.07	5.7	1.30	106	1.44
S317-50	1.92	0.11	5.7	2.19	114	2.82
S398-25	0.66	0.04	6.1	0.85	129	1.11
S398-40	1.43	0.08	5.6	1.47	103	1.99
S398-50	2.45	0.12	4.9	2.83	116	2.96
S587-25	0.53	0.03	5.6	0.34	64	0.63
S587-40	2.20	0.11	5.0	2.17	99	2.52
S587-50	3.73	0.14	3.8	3.97	106	4.25

After re-drying ($WA+Oven_{CS}$), CS recovered to 109.7 ± 21.6% of original values (paired *t*-test: $p = 0.033$). Recovery exceeded 100% for 8 of 12 compositions (range 63.8-141.6%). This is consistent with observations by Tajvidi et al. on CNF-bonded wood composites [19, 21]. The mechanism represents annealing: initial rapid drying traps a non-equilibrium fibril arrangement; the wet-dry cycle allows rearrangement into more favorable bonding configurations. Meng and Shi showed that hydrogen bond self-healing governs cellulose nanopaper performance [29]. This reversibility differs fundamentally from cement's irreversible C-S-H formation and suggests controlled wet-dry cycling as a post-processing conditioning step [30]. By the same logic, slower drying (e.g., ambient conditions) should approach the equilibrium fibril configuration directly, potentially achieving higher initial strength without requiring a wet-dry cycle - a hypothesis that warrants dedicated investigation [31].

To test whether a hydrophobic surface treatment could protect the material during subsequent wetting, a separate set of specimens was first hydrophobized (RAIN GUARD Eco-Pod) and then subjected to the same water-saturation and re-drying cycle (H + $WA+Oven_{CS}$ protocol). Hydrophobized-then-cycled specimens (H + $WA+Ove_{CS}$) recovered even more strength than their non-hydrophobized counterparts (paired *t*-test vs. non-hydrophobized: $p = 0.0001$). Several 50% CNF specimens reached the machine's load capacity (~ 52 kN).

2.6. Density-strength paradox

An inverse correlation was found between density and CS (Pearson correlation: $r = -0.768$, $p = 0.004$). Density ranged from 1.14–1.54 g/cm^3. Higher CNF content simultaneously reduces density (CNF is lighter than sand) and increases strength (more binder). This reversal versus conventional concrete highlights a different paradigm: binding efficiency per unit mass, not packing density, governs performance [3]. The same principle underlies CNF-bonded wood panels, where panels of lower density still met strength standards because performance was set by the quality of the hydrogen-bonded CNF network rather than by densification [32].

2.7. Post-peak ductility under wet conditions

In the standard wet compression protocol (WA + CS), tests were terminated at the first peak. To probe behaviour beyond this point, an extended protocol (WA+CS_2) was applied to 17 water-saturated specimens, in which loading continued past the first peak up to a 17 mm crosshead extension. Specimens did not fail catastrophically. Instead, after the initial peak (mean CS_{fp} = 0.10 ± 0.05 MPa), force decreased briefly and then rose monotonically as the specimens compacted. The rising regime began at a mean compaction strain of 44 ± 4% and continued to a mean strain of 56 ± 4% at the test endpoint (range 51–64%). The end-of-test force F_{end} exceeded the first-peak force F_{fp} by a factor of 4.2 ± 2.9 (range 1.0-9.9), with the largest amplification observed in 50% CNF specimens (mean F_{end}/F_{fp} = 6.7) and the smallest in 25% CNF specimens (mean 1.7). Apparent stress recalculated on the deformed cross-section reached up to 1.46 MPa for S398-50.

This response is qualitatively different from the brittle failure typical of cementitious materials and is consistent with the reversible hydrogen-bonding mechanism inferred from the wet-dry recovery experiments. Saturation eliminates the load-bearing CNF-CNF and CNF-sand bonds, causing the initial drop, but continued compaction expels free water, brings cellulose surfaces back into contact, and re-establishes the bonded skeleton under load. A comparable sequence, an initial post-peak drop followed by strengthening as the CNF network densifies and interfibrillar hydrogen bonds break and re-form, has been reported for compressed bulk CNF materials[33]. The mechanism is therefore inseparable from the mechanical interlocking discussed above: as bonds re-form, the compacted fibrillar network entraps sand particles, and the two contributions reinforce one another. Representative force-extension curves and the full WA+CS_2 dataset are provided as Supplementary Figure S8 and Supplementary Table S4. The implication for application is significant: in service conditions where wetting is unavoidable, CNF-sand composites would not fail catastrophically but would deform and partially recover load-bearing capacity, a behaviour more characteristic of a tough composite than of a conventional ceramic-bound matrix[34].

2.8. Flexural strength

FS ranged from 0.03 MPa (S587-25) to 1.17 MPa (S587-50) (Table 2, Supplementary Figure S4). FS correlated near-perfectly with CS (Pearson correlation: $r = 0.969$, $p < 0.001$): FS = 0.351 × CS − 0.065 (R^2 = 0.94) (Supplementary Figure S5). The FS/CS ratio (~ 0.30–0.35) exceeds typical OPC concrete (~ 0.10–0.15), indicating superior relative tensile performance from the fibrillar CNF network [35]. This elevated ratio reflects the role of the fibrils in bridging incipient cracks: unlike the brittle calcium-silicate-

hydrate phase of cement, the high-aspect-ratio CNF network sustains load across forming cracks and dissipates energy through fibril pull-out and interfibrillar slippage, the same plastic-deformation mechanism that underlies the ductile, non-catastrophic behaviour described above [34]. The anomalously low FS of S587-25 (0.03 MPa, CS = 0.53 MPa, CV = 20.7%) indicates marginal integrity at this composition.

2.9. Water absorption and hydrophobic treatment

Uncoated WA ranged from 23 to 31%, and after hydrophobic treatment from 15 to 22% (Table 4, Supplementary Figure S6). One-way ANOVA by CNF content was significant ($F = 11.93$, $p = 0.003$), with higher CNF content associated with lower WA, consistent with the denser fibrillar matrix at elevated binder content. The absorption kinetics were notably rapid: virtually all uptake occurred within the first 60 sec of immersion. This behaviour is characteristic of a highly porous, hygroscopic network. CNF is intrinsically hydrophilic due to abundant surface hydroxyl groups, and the pore network formed between sand grains at low CNF contents (25%) provides capillary pathways for rapid wicking [28]. At higher CNF contents (50%), the more complete fibrillar coating partially occludes inter-granular pores, explaining the modest but statistically significant reduction in WA. The instantaneous uptake profile also implies that WA is governed by capillary suction rather than diffusion, a finding with practical relevance, as it suggests that surface treatments must penetrate the pore network rather than merely coat the surface.

Table 4
Water absorption (WA) before and after hydrophobic treatment (WR). Δ = decrease in percentage points.

Sample	WA [%]	WA after WR [%]	Δ [pp]	Density [g/cm³]
S300-25	24	18	6	1.54
S300-40	30	18	12	1.36
S300-50	28	20	8	1.24
S317-25	26	17	9	1.45
S317-40	30	22	8	1.29
S317-50	28	21	7	1.14
S398-25	25	15	10	1.50
S398-40	28	22	6	1.25
S398-50	26	22	4	1.20
S587-25	27	18	9	1.53
S587-40	30	24	6	1.38
S587-50	28	21	7	1.20

2.10. Microstructural observations

Scanning electron microscopy (SEM) at 150× (Fig. 4) revealed the bonding mechanism and its compositional dependence. In specimens with 25% CNF (S300-25, Fig. 4a), individual sand grains (0.5-5 mm) are clearly distinguishable, with discrete fibrillar bridges spanning inter-granular contact zones. The CNF matrix forms thin menisci at grain contacts, consistent with a 'point-bonding' mechanism in which strength is governed by the number and cross-sectional area of load-bearing CNF bridges [21, 32]. The partial exposure of grain surfaces also explains the relatively high-water absorption at low CNF contents, as un-coated grain surfaces leave open capillary pathways.

At 50% CNF (S300-50, Fig. 4b), the microstructure is qualitatively different: a continuous, dense fibrillar film envelops the sand particles, forming a coherent binder matrix in which grains are embedded rather than bridged [21]. This transition from discrete bridging to continuous coating is consistent with the observed non-linear increase in CS between 25% and 50% CNF and explains why CNF_{eff} is a stronger predictor than either CNF% or solids% alone, it captures the absolute quantity of dry cellulose available to form this continuous phase. This microstructural picture also explains the lower bound on binder content: the S317-15 specimen (15% CNF), in which the fibrillar phase was too sparse to bridge and lock the sand grains, disintegrated on drying, whereas 25% CNF was sufficient to form a load-bearing point-bonded network. A minimum cellulose fraction of roughly 15–25% is therefore required to establish mechanical continuity, below which no coherent solid forms.

2.11. Summary of correlations

The Pearson correlation matrix (Supplementary Table S5) revealed: CS-FS near-perfect correlation (r = 0.969); all six CS protocols intercorrelated ($r > 0.89$); shrinkage as a potential quality indicator (r = 0.912 with CS); WA weakly correlated with CS (Pearson correlation: r = 0.333, p = 0.29), confirming different governing microstructural features.

Taken together, these relationships point to a single load-bearing phase. The near-perfect CS–FS coupling and the tight intercorrelation among all six compressive protocols indicate that one and the same hydrogen-bonded CNF network governs both compressive and flexural response, so a single mix parameter can be used to tune the full mechanical profile. The positive shrinkage–CS correlation is best read as an indirect effect rather than a causal one: higher CNF content produces both greater drying shrinkage and higher strength, so shrinkage serves as a convenient, non-destructive proxy for binder content and adequate consolidation. This contrasts with cast CNF films, where excessive or uneven drying shrinkage introduces moisture gradients and distortions that reduce mechanical performance; in the present granular composites the shrinkage instead tracks the amount of bonded cellulose [36]. Finally, the weak, non-significant WA–CS correlation confirms that water uptake and dry strength are governed by different features: strength by the quality of the bonded network, and water uptake by the open pore structure and capillary pathways.

3. Conclusions

This study demonstrates, for the first time, that entirely replacing cement with cellulose nanofibers as the sole binder in sand-based composites is feasible. The key findings are as follows:

(1) A minimum of ~ 25 wt% CNF is required for cohesion.

(2) Dry compressive strength ranges from 0.42 to 3.73 MPa, governed by CNF_{eff} (R^2 = 0.86); multiple regression explains 88.6% of variance.

(3) Reversible hydrogen bonding: water reduces CS to 5.8%, re-drying restores 109.7% (p = 0.033), with evidence of matrix consolidation. Mechanical interlocking likely contributes as a complementary mechanism: upon drying and self-condensation, CNFs form a continuous fibrous skeleton in which sand particles become physically entrapped, providing a load-transfer pathway that does not depend solely on the chemical bonding state.

(3a) Saturated specimens do not fail brittlely: under continued loading, force re-amplifies up to 4.2 ± 2.9 fold (and up to 9.9 fold for 50% CNF) at compaction strains of 51–64%, indicating substantial post-peak ductility (Supplementary Figure S8, Supplementary Table S4).

(4) Anisotropy ratio 1.47 (p = 0.0003) from preferential fibril alignment during compaction.

(5) FS/CS ratio ~ 0.35 exceeds OPC concrete, indicating superior relative tensile performance.

(6) Hydrophobic treatment reduces water absorption by 7.7 percentage points (p < 0.001).

The observed strength range (0.42–3.73 MPa) is below structural OPC concrete (> 20 MPa) but is well-suited to a range of non-structural applications where lightweight, low-embodied-carbon materials are desirable. Specific target niches include: decorative and landscape elements (garden edging blocks, pathway tiles, planters), where sustained mechanical loads are low and carbon footprint is a primary selection criterion; non-structural interior partition panels and infill tiles in dry environments; biodegradable temporary formwork or sacrificial moulds; and educational or demonstration prototypes in sustainable architecture. In each of these cases, the reversible hydrogen-bonding mechanism, which recovers and even exceeds original strength on re-drying, can be exploited as a feature rather than a limitation, for instance in self-healing or recyclable construction elements. Life cycle assessment (LCA) comparing CNF-sand composites against OPC concrete, rammed earth, and adobe across these application scenarios is a critical next step to quantify the actual environmental benefit.

Strengths of this study include its systematic factorial design, the first published characterisation of the CNF-sand system across a broad composition space, and the mechanistic interpretation supported by statistical analysis and microstructural observation. Limitations include non-standard specimen geometry (limiting direct comparison with standardised test data), limited FS replication (n = 1), the absence of cement-based reference specimens tested under identical conditions, and the restriction to a single sand gradation (0.5-5 mm). Future work should address: higher CNF solids (> 6%), larger standardised specimens, direct cement comparison at matched specimen geometry, long-term durability

(freeze-thaw, UV, biological degradation), life cycle assessment, WAXS for fibril orientation quantification, multi-cycle wet–dry conditioning, μCT for pore network characterisation, and nanoindentation for local mechanical property mapping. Alternative drying routes also warrant investigation: freeze-drying, by removing water via sublimation, bypasses the capillary forces that drive fibril consolidation during evaporative drying [31]. It would therefore be expected to preserve a more open, porous network rather than a dense bonded one, and comparative studies on bacterial nanocellulose have shown that freeze-dried samples are markedly less consolidated and mechanically weaker than oven- or air-dried counterparts [37]. Freeze-drying would thus serve as an informative control, clarifying how much of the strength reported here depends on capillary-driven consolidation rather than on the intrinsic fibril network, and how the drying pathway itself governs the final bonded structure. Hierarchical or layered architectures also merit dedicated study: a preliminary attempt to overlay a 4 mm pure-CNF layer (5.87 wt% solids) on a S300-40 base produced pronounced curvature on drying (a 'boat' shape with raised ends), indicating that differential shrinkage between the binder-rich layer and the bulk composite must be controlled before such designs can be exploited.

A further route to improved water resistance is the incorporation of a reactive silicate phase. Sodium silicate (water glass) can be hardened by exposure to gaseous CO_2, precipitating a silica gel that binds the grains while permanently sequestering CO_2 as sodium carbonate. Combining a CNF binder with a CO_2-cured silicate phase could therefore address the water sensitivity observed here while adding a carbon-storage function. We note, however, that incompletely carbonated sodium silicate can itself be moisture-sensitive owing to residual sodium ions; realising this approach would thus require ensuring complete carbonation or stabilising the silicate phase. This hybrid CNF–silicate system represents a promising direction for future work [38].

This work opens a new and promising research direction in sustainable, bio-based construction materials.

4. Materials and Methods

4.1. Materials

Cellulose nanofibers (CNF) were obtained from The Process Development Center, University of Maine. Per the manufacturer's SDS (Version 2, 2022-07-05): CAS 9004-34-6, particle width 5-200 nm, length 130 nm-225 μm, aspect ratio 14–23, crystallinity 67–88%, zeta potential − 48 to -5 mV, pH 7, decomposition > 349°C, thermal stability ~ 305°C [18]. As-received solids: 3.00 wt%. Additional solids (3.17%, 3.98%, 5.87%) were achieved by evaporative drying. Solids > 6.00% were unachievable under the adopted methodology. Sand fractions used: fine (0.1-2 mm) and coarse (0.5-5 mm).

4.2. Sample nomenclature and experimental design

Samples are designated S[solids]-[CNF%]; e.g., S300-25 = 3.00% solids, 25% CNF (Table 1). The primary matrix comprised 12 compositions − 4 solids × 3 ratios, all using 0.5-5 mm sand. Additionally: 3 fine-

sand variants (suffix F), 3 replicates (suffix R), and 1 disintegrated composition (S317-15) were tested.

Table 1
Sample nomenclature and compositions. All primary samples use 0.5-5 mm sand. CNF_{eff} = CNF% × solids%/100.

New name	Solids [%]	CNF [%]	Sand [%]	CNF_{eff} [%]
S300-25	3.00	25	75	0.75
S300-40	3.00	40	60	1.20
S300-50	3.00	50	50	1.50
S317-25	3.17	25	75	0.79
S317-40	3.17	40	60	1.27
S317-50	3.17	50	50	1.58
S398-25	3.98	25	75	0.99
S398-40	3.98	40	60	1.59
S398-50	3.98	50	50	1.99
S587-25	5.87	25	75	1.47
S587-40	5.87	40	60	2.35
S587-50	5.87	50	50	2.94

4.3. Sample preparation

Sand was oven-dried to constant mass and stored airtight. Ingredients were dosed by weight. Mixing: 60 sec with low speed, 30 sec pause, 60 sec high speed in a conventional 8-qt rotary mixer, where low and high speeds corresponded to approximately 60 and 135 rpm, respectively. Molds: 285 × 25 × 25 mm, detachable, no release agent (Supplementary Figure S1). Two-layer placement with manual tamping (24 × 24 mm wooden cuboid). No vibrating table was used, as CNF could accumulate in the upper layer due to lower density. Drying: 60°C for 24 h to constant weight (well the thermal stability threshold of ~ 305°C reported above). Storage: airtight containers.

4.4. Testing procedures and reference standards

Due to the exploratory nature of this study and the non-standard character of the material, testing procedures were adapted from established standards with modifications to accommodate specimen geometry and material behavior. No prior data existed; the testing program prioritized broad composition coverage over deep replication. CNFs are intrinsically anisotropic, with individual fibrils exhibiting higher stiffness along their axis [10, 39]. During compaction, high-aspect-ratio fibrils (14–23) are expected to align preferentially in the plane perpendicular to the tamping direction, which was confirmed experimentally (see Results) [19, 29, 40].

Compressive strength (CS): INSTRON 5900R, displacement-controlled at 2 mm/min, following principles of EN 12390-3 and ASTM C109 with non-standard specimen geometry (~ 25 × 25 × 25 mm cubes, exact dimensions measured individually; Supplementary Figure S7) [41, 42]. Six protocols tested (Supplementary Table S1). Dry CS: n = 3 per type. An additional protocol (WA+CS_2; n = 17 across all compositions except S587-25) was used to characterise post-peak behaviour: water-saturated specimens were loaded continuously past the first peak up to a 17 mm crosshead extension. Compaction strain ε is defined as the relative reduction in specimen height, $(h_0 - h)/h_0$; ε_{onset} denotes the strain at which force begins to rise again after the first peak, and ε_{end} the strain at the test endpoint.

Flexural strength (FS): three-point bending, L = 90 mm, per principles of EN 12390-5/ASTM C348. FS = $3FL/(2bd^2)$ [43, 44]. One specimen per type (n = 1). This limited replication is justified: the primary objective was to establish whether CNF-sand composites exhibit measurable flexural capacity across the entire composition space. The strong correlation subsequently observed between FS and CS (r = 0.969, p < 0.001) supports reliability; however, future studies must increase sample sizes.

Water absorption (WA): per principles of EN 13755/ASTM C642 [45, 46]. Two specimens per type. Half-depth submersion for 30 min then full submersion; measured at 0, 60 sec, 5, 15, 30, 60 min. WA = $(m_{wet} - m_{dry})/m_{dry} \times 100\%$. Hydrophobic treatment: RAIN GUARD Eco-Pod Waterproofer, 10 sec immersion, 7 days cure.

Scanning electron microscopy (SEM): AMRay 1820 iXRF EDS (15 kV, 150×) and Zeiss NVision 40 FIB/SEM (10 kV, 150×). Optical microscopy performed on all types.

4.5. Statistical analysis

Python 3 (SciPy, NumPy, Pandas). Descriptive statistics for CS (n = 3). One-way ANOVA, post-hoc t-tests, Pearson correlations, linear and multiple regression. Effective dry CNF content: CNF_{eff} = CNF% × solids%/100. Significance level: α = 0.05. All tests were two-tailed. Given the small samples (n = 3 per composition), the normality assumption could not be tested reliably; one-way ANOVA was used to compare the three CNF-content groups instead of multiple pairwise t-tests to control the Type I error rate, and reported pairwise comparisons should be read as exploratory. Exact P values are reported throughout; the terms ‘significant’ and ‘substantial’ are used only where accompanied by a P value. Unless stated otherwise, values following the ± sign are standard deviations (s.d.).

Declarations

Competing Interests

The authors declare no competing interests.

Author Contribution

M.S. (Małgorzata Szafraniec): Conceptualization (supporting); Data curation (lead); Formal analysis (supporting); Funding acquisition (supporting); Investigation (lead); Methodology (lead); Project administration (lead); Visualization (lead); Writing – original draft (lead); Writing – review & editing (equal).

L.L. (Linfei Li): Validation (lead); Formal analysis (lead); Writing – review & editing (equal).

E.N.L. (Eric N. Landis): Conceptualization (lead); Resources (lead); Supervision (lead); Funding acquisition (lead); Writing – review & editing (equal).

Acknowledgement

This work was carried out during a research stay entitled "Research on cement-based composite materials with a focus on nanocellulose to enhance cement-based composite materials" at the Department of Civil and Environmental Engineering, University of Maine, Orono, USA, under the supervision of Prof. Eric N. Landis, Ph.D., P.E. The stay was funded by the Polish National Agency for Academic Exchange (NAWA) under the STER programme, "Internationalization of Doctoral Schools", through the project "Internationalization of the Doctoral School of Lublin University of Technology, IDeaS of LUT". The authors thank The Process Development Center at the University of Maine for providing the cellulose nanofiber material, and Prof. Mehdi Tajvidi for valuable discussions on cellulose nanofiber binding mechanisms. This work was financially supported by the Ministry of Science and Higher Education, Poland, under grant number FD-IL-068.

Data Availability

All data generated or analysed during this study are included in this published article and its supplementary information files.

References

1. Hasanbeigi, A., Price, L. & Lin, E. Emerging energy-efficiency and CO2 emission-reduction technologies for cement and concrete production: A technical review. *Renew. Sustain. Energy Rev.* **16**, 6220–6238. https://doi.org/10.1016/j.rser.2012.07.019 (2012).
2. Shah, I. H., Miller, S. A., Jiang, D. & Myers, R. J. Cement substitution with secondary materials can reduce annual global CO2 emissions by up to 1.3 gigatons. *Nature Communications 2022 13:1* 13, 1–11; (2022). https://doi.org/10.1038/s41467-022-33289-7
3. Neville, A. M. *Properties of Concrete* (Stowarzyszenie Producentów Cementu, 2012). 10.1139/l97-107
4. Favier, A., De Wolf, C., Scrivener, K., Habert, G. & Industry, C. A sustainable future for the European Cement and (2018). https://doi.org/10.3929/ethz-b-000301843

5. Singh, B., Ishwarya, G., Gupta, M. & Bhattacharyya, S. K. Geopolymer concrete: A review of some recent developments. *Constr. Build. Mater.* **85**, 78–90. https://doi.org/10.1016/j.conbuildmat.2015.03.036 (2015).
6. Roy, P. et al. Production Cost of Biocarbon and Biocomposite, and Their Prospects in Sustainable Biobased Industries. *Sustain. (Switzerland)*. **16**, 5633. https://doi.org/10.3390/su16135633 (2024).
7. Seymour, R. S. The northeastern region. *Reg. silviculture United States*. **3**, 31–79 (1995).
8. Seddiqi, H. et al. Cellulose and its derivatives: towards biomedical applications. *Cellulose 2021 28:4* 28, 1893–; (1931). https://doi.org/10.1007/s10570-020-03674-w (2021).
9. Jung, Y. H. et al. High-performance green flexible electronics based on biodegradable cellulose nanofibril paper. *Nature Communications 2015 6:1* 6, 1–11; (2015). https://doi.org/10.1038/ncomms8170
10. Moon, R. J., Martini, A., Nairn, J., Simonsen, J. & Youngblood, J. Cellulose Nanomaterials Review: Structure, Properties and Nanocomposites. *Chem. Soc. Rev.* **40**, 3941–3994. https://doi.org/10.1039/c0cs00108b (2011).
11. Tasnim, R., Wang, L., Parit, M. & Zhang, Y. J. Interactions of Cellulose Nanofibrils with a Foliar Fertilizer and Wild Blueberry Leaves: Potential to Enhance Fruit Yield. *ACS Agricultural Sci. Technol.* **2**, 712–718. https://doi.org/10.1021/acsagscitech.2c00118 (2022).
12. Ramanathan, S., Chopperla, K. S. T., Washington, T., Isgor, O. B. & Weiss, W. J. Cellulose Nanocrystals as an Additive for Prestressed Concrete Slab Girders. *Precast/Prestresses Concrete Institue, Chicago* (2023).
13. Chopperla, K. S. T., Ramanathan, S., Moon, R. J., Isgor, O. B. & Weiss, W. J. Field Demonstrations Using Cellulose Nanomaterials as Concrete Additives. *Concr. Int.* **45**, 33–38. 10.14359/51738464 (2023).
14. Aziz, M. A., Zubair, M. & Saleem, M. Development and testing of cellulose nanocrystal-based concrete. *Case Stud. Constr. Mater.* **15**, e00761. https://doi.org/10.1016/j.cscm.2021.e00761 (2021).
15. Kamasamudram, K. S., Ashraf, W., Landis, E. N. & Khan, R. I. Effects of ligno– and delignified–cellulose nanofibrils on the performance of cement-based materials. *J. Mater. Res. Technol.* **13**, 321–335. https://doi.org/10.1016/j.jmrt.2021.04.090 (2021).
16. Kamasamudram, K. S., Ashraf, W. & Landis, E. N. Cellulose nanofibrils with and without nanosilica for the performance enhancement of Portland cement systems. *Constr. Build. Mater.* **285**, 121547. https://doi.org/10.1016/j.conbuildmat.2020.121547 (2021).
17. Kolour, H. H., Ashraf, W. & Landis, E. N. Hydration and early age properties of cement pastes modified with cellulose nanofibrils. *Transp. Res. Rec*. **2675**, 38–46. https://doi.org/10.1177/0361198120945993 (2021).
18. University of Maine PDC. Cellulose Nanofibril Safety Data Sheet, Version 2 (2022). https://secure.touchnet.com/C22921_ustores/web/product_detail.jsp?PRODUCTID=2995&SINGLESTORE=true

19. Tajvidi, M., Gardner, D. J. & Bousfield, D. W. Cellulose Nanomaterials as Binders: Laminate and Particulate Systems. *J. Renew. Mater.* **4**, 365–376. https://doi.org/10.7569/JRM.2016.634103 (2016).
20. US20150033983A1. - Composite building products bound with cellulose nanofibers - Google Patents. https://patents.google.com/patent/US20150033983A1/en
21. Tayeb, A. H., Amini, E., Ghasemi, S. & Tajvidi, M. Cellulose Nanomaterials—Binding Properties and Applications: A Review. *Molecules 2018*. **23**, 2684. https://doi.org/10.3390/molecules23102684 (2018).
22. Jiang, F., Hsieh, Y. & Lo Self-assembling of TEMPO Oxidized Cellulose Nanofibrils As Affected by Protonation of Surface Carboxyls and Drying Methods. *ACS Sustain. Chem. Eng.* **4**, 1041–1049. https://doi.org/10.1021/acssuschemeng.5b01123 (2016).
23. Bui, Q. B., Morel, J. C., Hans, S. & Meunier, N. Compression behaviour of non-industrial materials in civil engineering by three scale experiments: the case of rammed earth. *Materials and Structures 2008 42:8* 42, 1101–1116; (2008). https://doi.org/10.1617/s11527-008-9446-y
24. Silveira, D. et al. Mechanical properties of adobe bricks in ancient constructions. *Constr. Build. Mater.* **28**, 36–44. https://doi.org/10.1016/j.conbuildmat.2011.08.046 (2012).
25. Rol, F., Rouilly, A. & Bras, J. Thermo-compression of cellulose nanofibrils. *Cellulose* 27, 25–40; (2019). https://doi.org/10.1007/s10570-019-02720-6 (2019).
26. Pintiaux, T., Viet, D., Vandenbossche, V., Rigal, L. & Rouilly, A. High Pressure Compression-Molding of α-Cellulose and Effects of Operating Conditions. *Materials 2013, Vol. 6, Pages 2240–2261* 6, 2240–2261; (2013). https://doi.org/10.3390/ma6062240
27. Pintiaux, T., Viet, D., Vandenbossche, V., Rigal, L. & Rouilly, A. Binderless materials obtained by thermo-compressive processing of lignocellulosic fibers: A Comprehensive review. *Bioresources* **10**, 1915–1963. 10.15376/biores.10.1.1915-1963 (2015).
28. Lindman, B., Karlström, G. & Stigsson, L. On the mechanism of dissolution of cellulose. *J. Mol. Liq*. **156**, 76–81. 10.1016/j.molliq.2010.04.016 (2010).
29. Meng, Q. & Shi, X. A microstructure-based constitutive model of anisotropic cellulose nanopaper with aligned nanofibers. *Extreme Mech. Lett.* **43**, 101158. 10.1016/j.eml.2020.101158 (2021).
30. Taylor, H. F. Cement chemistry. *Vol. 2. London: Thomas Telford*; (1997). https://doi.org/10.1680/cc.25929
31. Sinquefield, S., Ciesielski, P. N., Li, K., Gardner, D. J. & Ozcan, S. Nanocellulose Dewatering and Drying: Current State and Future Perspectives. *ACS Sustain. Chem. Eng.* **8**, 9601–9615. https://doi.org/10.1021/acssuschemeng.0c01797 (2020).
32. Amini, E., Tajvidi, M., Gardner, D. J. & Bousfield, D. W. Utilization of cellulose nanofibrils as a binder for particleboard manufacture. *Bioresources* **12, 4093;** (10.15376). 10.15376/biores.12.2.4093-4110 (2017).
33. Guan, Q. F. et al. Lightweight, tough, and sustainable cellulose nanofiber-derived bulk structural materials with low thermal expansion coefficient. *Sci. Adv.* **6** (18), eaaz1114.

10.1126/sciadv.aaz1114 (2020).

34. Larsson, P. A., Berglund, L. A. & Wågberg, L. Ductile All-Cellulose Nanocomposite Films Fabricated from Core–Shell Structured Cellulose Nanofibrils. *Biomacromolecules* **15**, 2218–2223. https://doi.org/10.1021/bm500360c (2014).
35. 318 – 19(22). Building Code Requirements for Structural Concrete and Commentary (Reapproved 2022). https://www.concrete.org/publications/internationalconcreteabstractsportal.aspx?m=details&ID=51716937
36. Baez, C., Considine, J. & Rowlands, R. Influence of drying restraint on physical and mechanical properties of nanofibrillated cellulose films. *Cellulose 2014 21:1* 21, 347–356; (2014). https://doi.org/10.1007/s10570-013-0159-1
37. Andree, V. et al. Influence of drying methods on the physical properties of bacterial nanocellulose. *Mater. Res. Express*. **8**, 025402. 10.1088/2053 - 1591/abe016 (2021).
38. Statkauskas, M., Vaičiukynienė, D., Grinys, A. & Bajare, D. Effect of sodium silicate and sodium hydroxide ratios on compressive strength of ceramic brick and metakaolin waste-based geopolymer binder. *Materials* **18**, 4947. https://doi.org/10.3390/ma18214947 (2025).
39. Li, K. et al. Alignment of Cellulose Nanofibers: Harnessing Nanoscale Properties to Macroscale Benefits. *ACS Nano*. **15**, 3646–3673. https://doi.org/10.1021/acsnano.0c07613 (2021).
40. Roozbahani, S., Hamilton, J., Alsamsam, O., Mason, M. & Tilbury, K. B. Induction and quantification of cellulose nanofibril alignment in nano-hydroxyapatite biocomposite films. *Research Square*; (2022). https://doi.org/10.21203/RS.3.RS-1420521/V1
41. European Committee for Standardization. *EN 12390-3:2019-07. Testing Hardened Concrete-Part 3: Compressive Strength of Test Specimens* Vol. (Brussels, 2019).
42. Test Method for Compressive Strength of Hydraulic Cement Mortars. (Using 2-in. or [50mm] Cube Specimens). (2021). https://doi.org/10.1520/C0109_C0109M-21 doi:10.1520/C0109_C0109M-21.
43. *EN 12390-5:2019-08. Testing Hardened Concrete-Part 5: Flexural Strength of Test Specimens*.
44. Test Method for Flexural Strength of Hydraulic. -Cement Mortars; (2021). https://doi.org/10.1520/C0348-21
45. Polish Committee for Standardization. *PN-EN 13755:2008. Natural Stone Test Methods - Determination of Water Absorption at Atmospheric Pressure* Vol. (Warsaw, 2008).
46. Test Method for. Density, Absorption, and Voids in Hardened Concrete; (2021). https://doi.org/10.1520/C0642-21

Figures

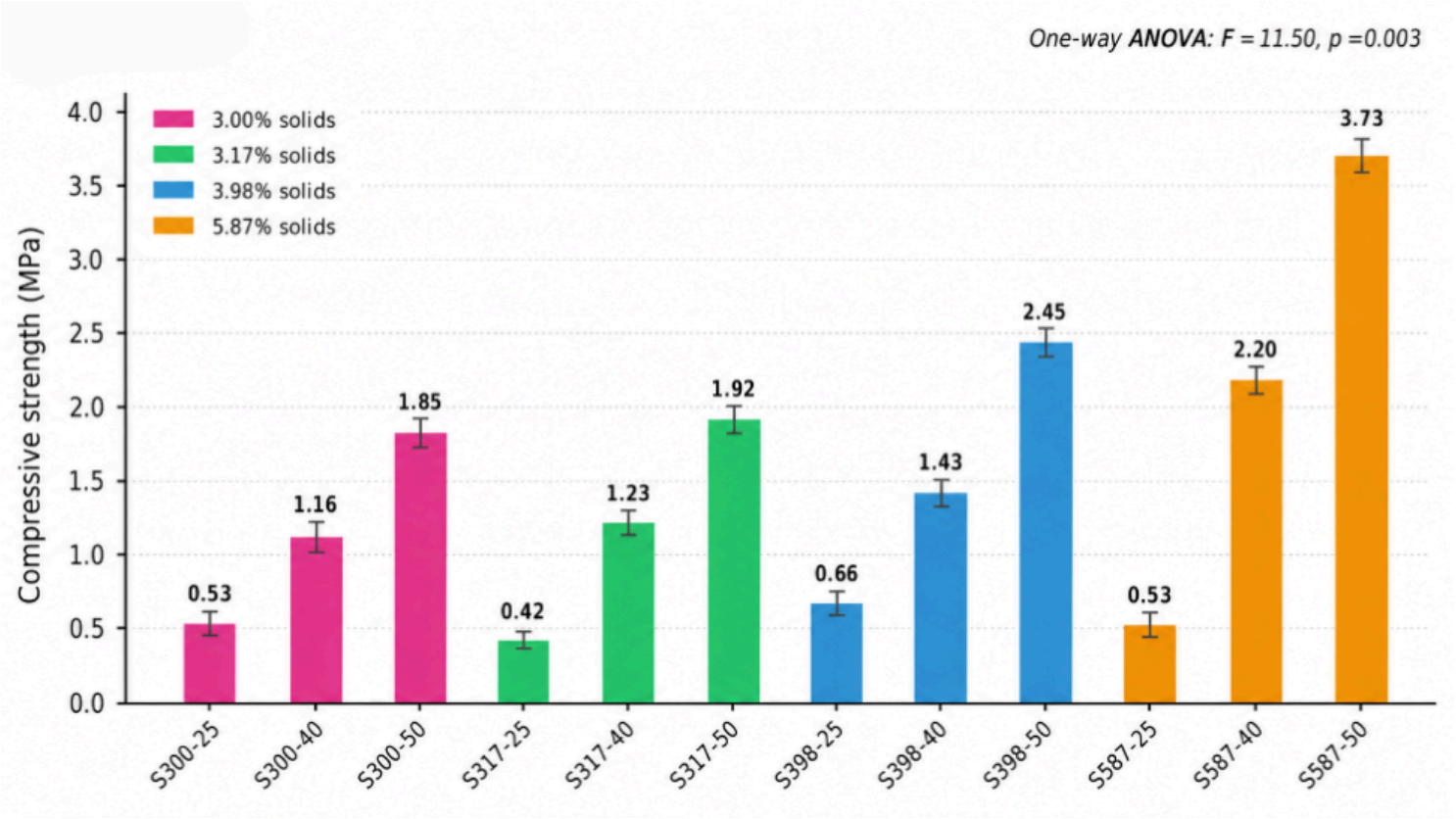


Figure 1

Dry compressive strength (CS) of CNF-sand composites. Bars show mean ± s.d. (*n* = 3). Colour: pink, 3.00% solids; green, 3.17%; blue, 3.98%; gold, 5.87%. Values above bars are mean CS (MPa). One-way ANOVA: $F = 11.50$, $p = 0.003$. Error bars, ± s.d. Numerical values are given in Table 2.

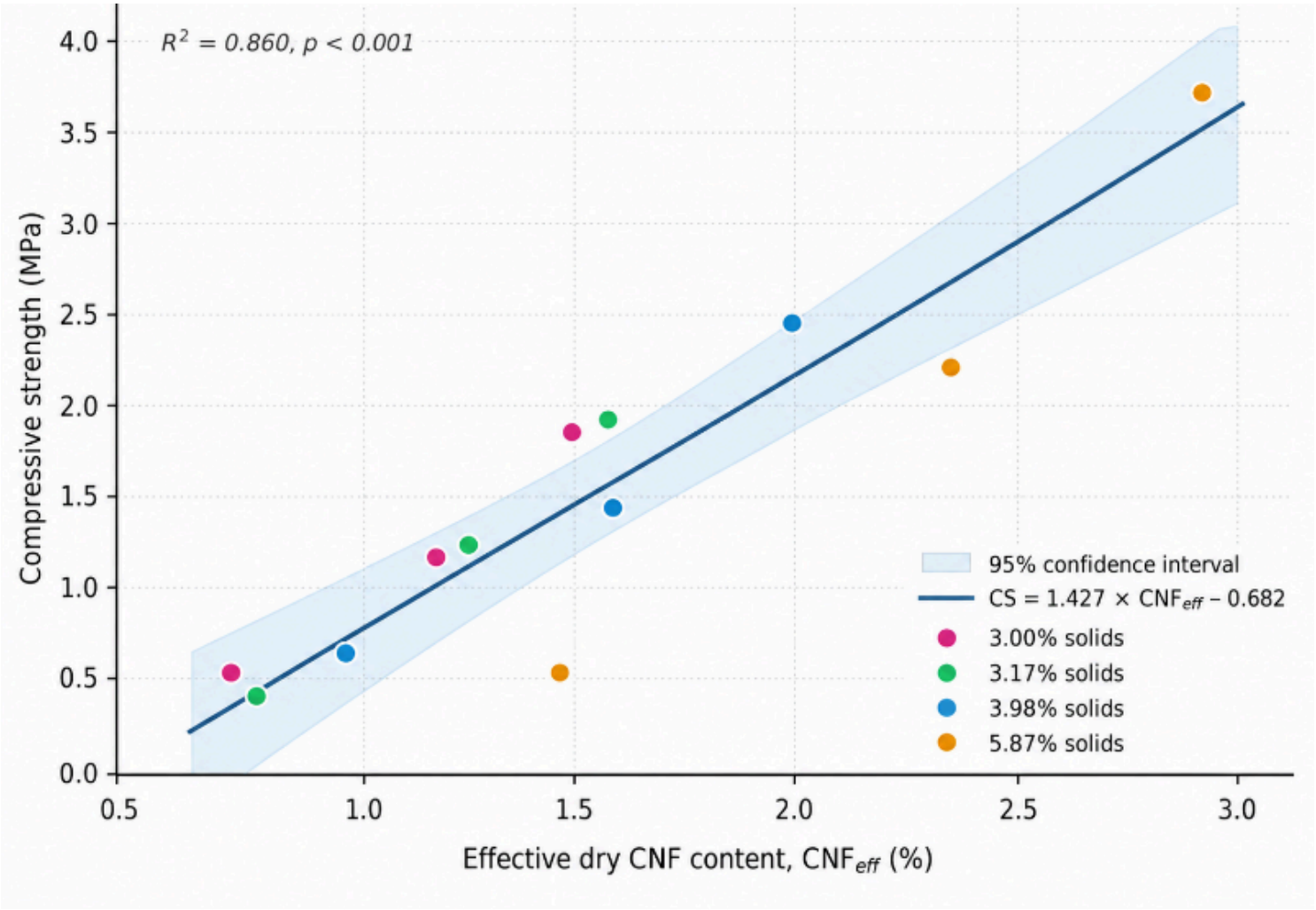


Figure 2

Compressive strength (CS) versus effective dry CNF content (CNF_{eff}). CNF_{eff} = CNF% × solids%/100. Colours as in Figure 1. Solid line: CS = 1.427 × CNF_{eff} – 0.682; shaded band: 95% confidence interval. R^2 = 0.860, p < 0.001.

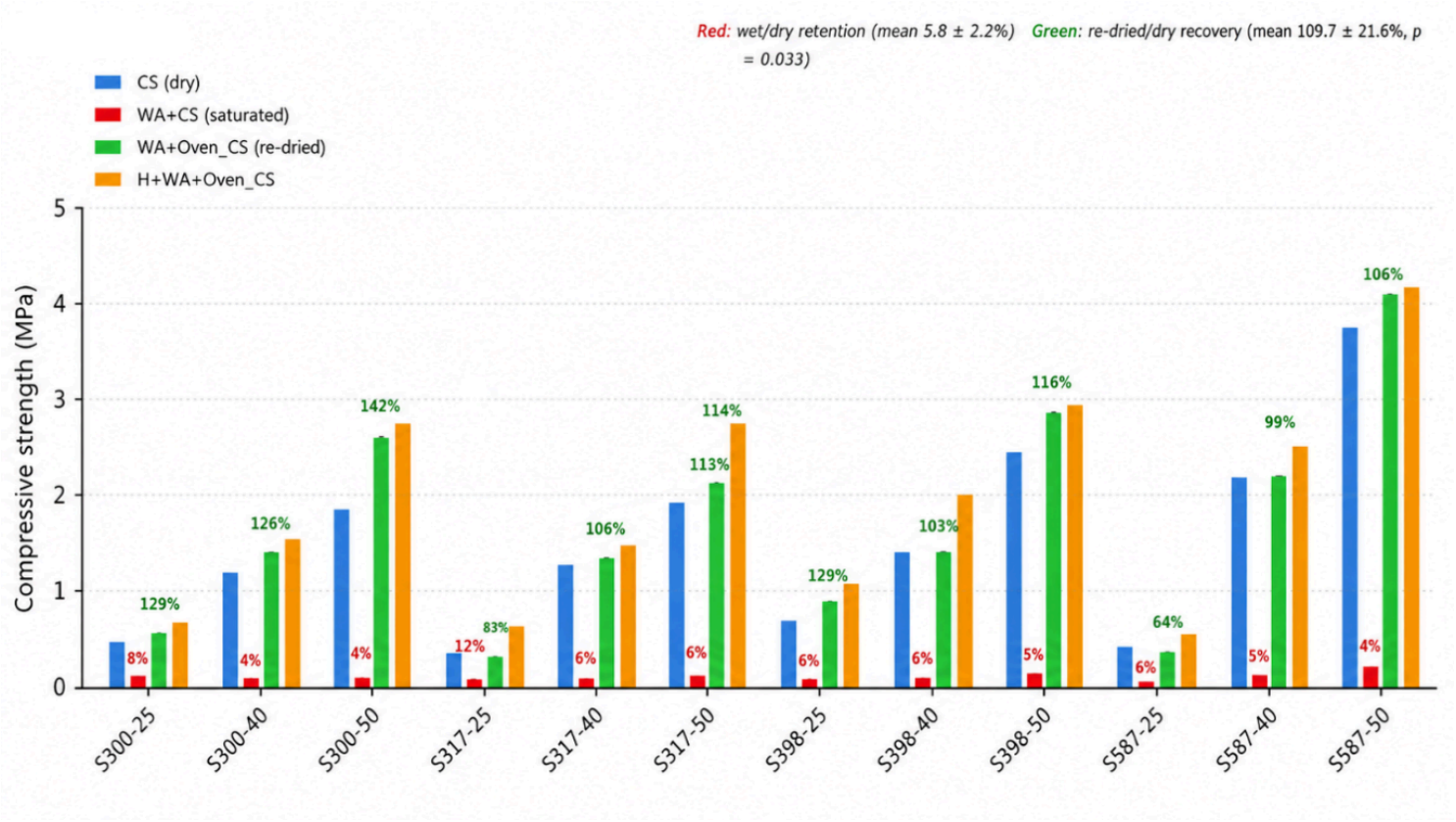


Figure 3

Effect of water cycling on compressive strength of all 12 primary compositions. Grouped bars: CS (dry, blue), WA+CS (saturated, red), WA+Oven$_{CS}$ (re-dried, green), H+WA+Oven$_{CS}$ (hydrophobized then cycled, gold). Bars, mean; error bars, ± s.d. (n = 3 for CS; n = 2 for WA protocols). Red percentages: wet/dry retention; green: re-dried/dry recovery. Mean retention 5.8 ± 2.2%; mean recovery 109.7 ± 21.6% (paired t-test: p = 0.033).

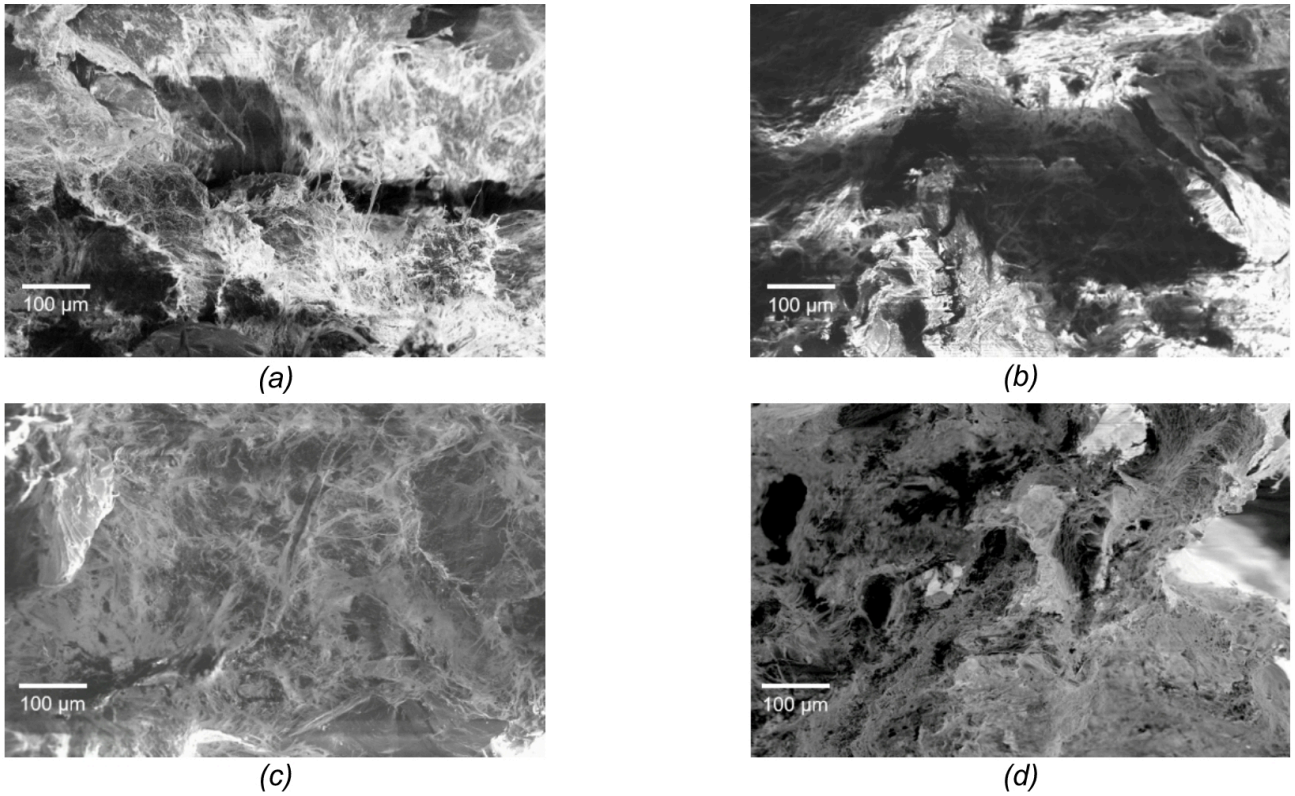


Figure 4

SEM micrographs (150×) showing CNF-sand bonding mechanism. (**a**) S300-25 (25% CNF): discrete fibrillar bridges at grain contacts (point-bonding). (**b**) S300-50 (50% CNF): continuous fibrillar matrix embedding particles. (**c**) Post-compression fracture: fibril pull-out at CNF-sand interface. (**d**) Re-dried S300-50: compacted network consistent with CS recovery after wet-dry cycling. Scale bars: 100 µm (**a**-**c**). AMRay 1820 iXRF EDS (15 kV); Zeiss NVision 40 FIB/SEM (10 kV).

Supplementary Files

This is a list of supplementary files associated with this preprint. Click to download.

- SupplementaryInformationSR.docx